A&A 642, A136 (2020)
https://doi.org/10.1051/0004-6361/202037916

Astronomy & Astrophysics

Cygnus survey with the Giant Metrewave Radio Telescope at 325 and 610 MHz: the catalog*

P. Benaglia[1,2], C. H. Ishwara-Chandra[3], H. Intema[4,5], M. E. Colazo[6], and M. Gaikwad[7]

[1] Instituto Argentino de Radioastronomía, CONICET & CICPBA, CC5 (1897) Villa Elisa, Prov. de Buenos Aires, Argentina
e-mail: paula@iar.unlp.edu.ar
[2] Facultad de Ciencias Astronómicas y Geofísicas, UNLP, Paseo del Bosque s/n, 1900 La Plata, Argentina
[3] National Centre for Radio Astrophysics (NCRA-TIFR), Pune 411 007, India
[4] International Centre for Radio Astronomy Research, Curtin University, Bentley, WA 6102, Australia
[5] Leiden Observatory, Leiden University, Niels Bohrweg 2, 2333 CA Leiden, The Netherlands
[6] Comisión Nacional de Actividades Espaciales, Paseo Colón 751, (1063) CABA, Argentina
[7] Max-Planck-Institut für Radioastronomie, Auf dem Hügel 69, 53121 Bonn, Germany

Received 8 March 2020 / Accepted 23 July 2020

ABSTRACT

Context. Observations at the radio continuum band below the gigahertz band are key when the nature and properties of nonthermal sources are investigated because their radio radiation is strongest at these frequencies. The low radio frequency range is therefore the best to spot possible counterparts to very high-energy (VHE) sources: relativistic particles of the same population are likely to be involved in radio and high-energy radiation processes. Some of these counterparts to VHE sources can be stellar sources.
Aims. The Cygnus region in the northern sky is one of the richest in this type of sources that are potential counterparts to VHE sources. We surveyed the central ∼15 sq deg of the Cygnus constellation at the 325 and 610 MHz bands with angular resolutions and sensitivities of 10″ and 6″, and 0.5 and 0.2 mJy beam^{-1}, respectively.
Methods. The data were collected during 172 h in 2013–2017, using the Giant Metrewave Radio Telescope with 32 MHz bandwidth, and were calibrated using the SPAM routines. The source extraction was carried out with the PyBDSF tool, followed by verification through visual inspection of every putative catalog candidate source in order to determine its reliability.
Results. In this first paper we present the catalog of sources, consisting of 1048 sources at 325 MHz and 2796 sources at 610 MHz. By cross-matching the sources from both frequencies with the objects of the SIMBAD database, we found possible counterparts for 143 of them. Most of the sources from the 325-MHz catalog (993) were detected at the 610 MHz band, and their spectral index α was computed adopting $S(\nu) \propto \nu^{\alpha}$. The maximum of the spectral index distribution is at $\alpha = -1$, which is characteristic of nonthermal emitters and might indicate an extragalactic population.

Key words. catalogs – radio continuum: general – open clusters and associations: individual: Cyg OB2 – open clusters and associations: individual: Cyg OB8 – open clusters and associations: individual: Cyg OB9

1. Introduction

The first gamma-ray all-sky observations, obtained decades ago with the satellites COS-B (Hermsen et al. 1977, and references therein) and Compton (Hartman et al. 1999), disclosed numerous sources with no counterpart at other wavelengths. These are hereafter called unidentified gamma-ray sources, or UNIDS. Since then, a large number of multifrequency observations have been implemented to understand the nature of these sources (e.g., Paredes et al. 2008; Massaro et al. 2013). Despite significant improvement in the telescope capabilities in sensitivity and resolution, there still remain thousands of gamma-ray sources to be identified. For instance, the fourth catalog of the *Fermi* Large Area Telescope (The Fermi-LAT collaboration 2020, more than 5000 sources) listed about one-third of the detected sources without any counterpart at lower energies. The sources that were detected with ground-based telescopes, at TeV energies, also present problems in conclusive identification; in addition, the high uncertainty on their position precludes the correlation with individual objects (see, e.g., the High Energy Stereoscopic System, H.E.S.S., source catalog[1] and its identifications).

The identified gamma-ray sources are mostly active galactic nuclei, AGNs, and pulsars, supernova remnants, or high-mass X-ray binaries (HMXBs). These objects emit at radio wavelengths and are generally stronger at low radio frequencies (<1 GHz) as a result of the nature of the spectra of synchrotron radiation. In this part of the electromagnetic spectrum, major catalogs and surveys lack angular resolution or sensitivity to seek for singular counterparts of UNIDS (e.g., the National Radio Astronomy Observatory Very Large Array Sky Survey, NVSS, ∼45″ and 1 mJy, or the Westerbork Northern Sky Survey, ∼54″ and 3 mJy; Condon et al. 1998; Rengelink et al. 1997). Recently, other types of stellar sources have been proposed as possible gamma-ray emitters, and different scenarios were analyzed. In addition to the well-studied microquasars (Romero et al. 2003), colliding-wind binaries (Benaglia & Romero 2003), Herbig Haro objects, young stellar objects (YSO), (Bosch-Ramon et al. 2010; Araudo et al. 2007; Rodríguez-Kamenetzky et al. 2019),

* Full Tables 3–5 are only available at the CDS via anonymous ftp to cdsarc.u-strasbg.fr (130.79.128.5) or via http://cdsarc.u-strasbg.fr/viz-bin/cat/J/A+A/642/A136

[1] https://www.mpi-hd.mpg.de/hfm/HESS/pages/home/sources/

and stellar bow shocks (Benaglia et al. 2010; del Valle & Pohl 2018; del Palacio et al. 2018) are capable of producing gamma-rays. A signature of high-energy emission is nonthermal radio emission because particles from the same population are likely to be involved in processes at both energy ranges, at the radio through synchrotron process, and at VHE emission through inverse-Compton scattering. Moreover, the determination of counterparts of gamma-ray sources through radio observations in star-forming regions will help to clarify the role of young stars and collective wind effects in the acceleration of galactic cosmic rays (e.g., Romero et al. 2008).

Various high-energy sources have been detected in the northern-sky Cygnus rift, a large region with star-formation activity that is one of the richest and most crowded in stellar objects in the Galaxy. Many thousand sources are cataloged in the literature in this region, and more than half are stars. The high absorption in the line of sight, however, prevents accurate mapping of the stellar population at the optical and IR ranges. Low-frequency (centimeter wavelengths) observations are the only way to probe nonthermal radio emission, and this emission travels practically unabsorbed; observing facilities that provide high angular resolution and sensitivity are crucial. In this line, the Giant Metrewave Radio Telescope (GMRT) is ideal for sampling the sky to search for emission of stellar sources: it operates between 150 and 1400 MHz, with baselines along 25 km that allow images with an angular resolution of a few arcseconds (Swarup et al. 1991).

We carried out a survey of the center of the Cygnus rift with the GMRT by means of continuum observations at two bands (325 MHz and 610 MHz) to investigate the nonthermal emission of various types of sources that lie in this rich field and are potential counterparts of UNIDS. With two frequencies, we were also able to obtain spectral information that might help to categorize certain classes and emission mechanisms on the basis of the spectral index. We present the source catalog at each band here, along with spectral index information when possible. In Sect. 2 we present the main characteristics of the Cygnus region and precedent studies at low-frequency radio continuum; in Sects. 3 and 4 we describe how the observations were carried out, and the processes attached to the data reduction to obtain the final images. Section 5 explains the data analysis we performed on the images and how the sources were extracted. Section 6 contains the findings related to spectral indices for the sources we detected at the two observing bands. In Sect. 7 we discuss the main properties of the catalog. Results of the search for counterparts are given in Sect. 8, and we conclude by mentioning related studies and prospects in the last section.

2. Cygnus region and background of the radio observations

The Cygnus rift is a large area at northern declination that is obscured by the dust of molecular clouds. It spans from $65° \leq l \leq 95°$, $-8° \leq b \leq +8°$ at a distance up to 2.5 kpc; see Reipurth et al. (2008) for a comprehensive review. As portrayed in Fig. 1 (Mahy et al. 2013), it encompasses nine OB associations and several bright open clusters, with signs of recent star formation. One of the youngest associations is Cyg OB2: it is also the richest association, with more than one hundred O stars and thousands of B stars, as reported by Knödlseder (2000). Next to OB2, Cyg OB8 and Cyg OB9 present hundreds of hot stars.

The main goal of the project was to relate nonthermal radio sources with stellar objects, that is, stars at different evolutionary stages: we circumscribed the region under study to the associations Cyg OB2, OB8 and OB9; its extension is displayed in Fig. 1 in Galactic coordinates, related to the Cygnus constellation. It covers ∼15 sq deg. The associations Cyg OB8 and OB9 are not surveyed in full because they are adjacent to strong and/or large sources (like the cases of Cyg X–1 and Cyg A), which might introduce problems related to imaging of a highly dynamic range.

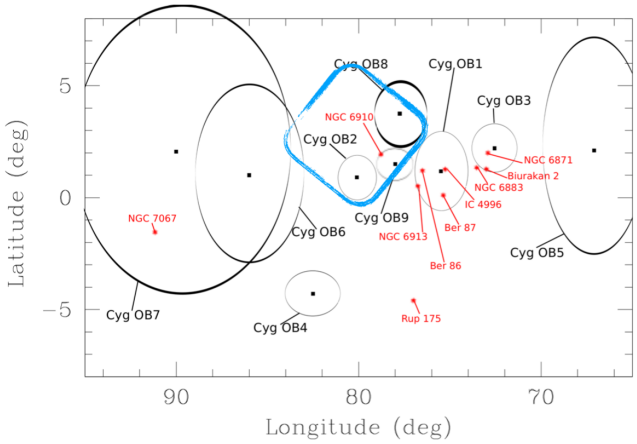

Fig. 1. Observed area of the Cygnus constellation marked with a blue contour box, over the stellar associations and bright clusters from Mahy et al. (2013).

Below the Jansky threshold, the Cygnus area was observed as part of Galactic plane surveys with the Very Large Array[2] by Garwood et al. (1988) at 1.4 GHz continuum, at $b = 0°$, a resolution up to 4″, and completely to a peak flux density of about 30 mJy. The results were complemented by those of Zoonematkermani et al. (1990) for $|b| < 0.8°$, which provided angular resolution and flux limit alike. With the Texas Interferometer, Douglas et al. (1996) imaged the area at the arcsecond scale above flux densities of 0.25–0.4 Jy. Taylor et al. (1996) carried out Westerbork Synthesis Radio Telescope observations along the Galactic plane and for $|b| < 1.6°$, at an angular resolution of ∼1′. They detected sources brighter than 10 mJy beam^{-1}.

In particular, Setia Gunawan et al. (2003) published the Westerbork Synthesis Radio Telescope 1400 and 325 MHz continuum survey of Cyg OB2, which attained angular resolutions of 13″ and 55″ and 5 σ flux density limits of ∼2 mJy and ∼10–15 mJy, respectively. In an observed area of $2° \times 2°$, the authors detected 210 discrete sources, 98 of them at both frequencies. They also detected 28 resolved sources.

The observations presented here were performed at two bands with the GMRT, centered at 325 and 610 MHz. This allowed us to map the continuum radio emission at arcsecond resolution and below the mJy sensitivity level. Some information about the observations has been given in Ishwara-Chandra et al. (2019).

3. Observations

The observed region marked in Fig. 1 is displayed in equatorial coordinates in Fig. 2. The half-power beam widths of the GMRT fields of view (FoVs) are $81 \pm 4'$ at 325 MHz and $43 \pm 3'$ at 610 MHz[3].

To cover the desired observing area, we needed to point at 5 FoVs of 325 MHz and 47 FoVs of 610 MHz. Some observations

[2] https://science.nrao.edu/facilities/vla

[3] GMRT Observer's Manual; http://www.ncra.tifr.res.in/ncra/gmrt/gmrt-users/observing-help/manual_7jul15.pdf

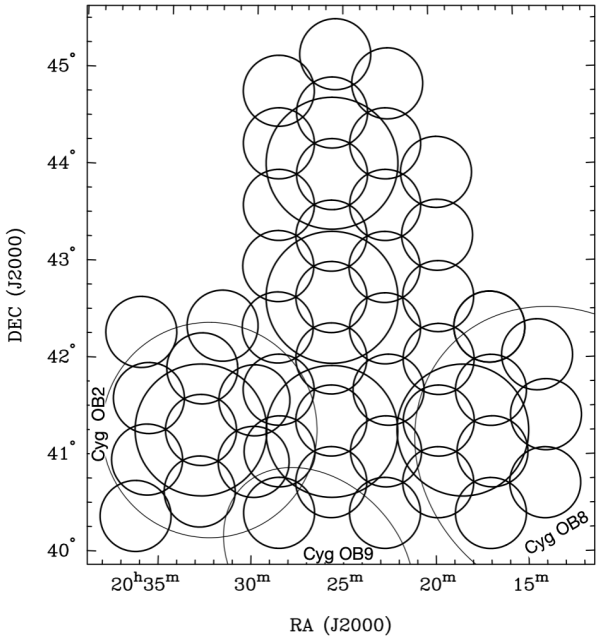

Fig. 2. Disposition of the pointings at 325 MHz (larger circles) and 610 MHz (smaller circles), showing the observed FoV half-power beam widths. The extent of the stellar associations Cyg OB2, OB8, and OB9 (Uyanıker et al. 2001) is shown using thinner lines.

Table 1. Observing campaigns basic information.

#	Campaing ID	Time (h)	Obs. dates
1	25_026	12	2013
2	27_036	40	2014–2015
3	28_081	40	2015
4	30_027	60	2016–2017

consisted of bad data, so that we repeated them with new observations (20 h). The layout of the pointings was chosen to yield a uniform noise while minimizing the number of them (i.e., the observing time). Figure 2 shows the disposition of the pointings and the FoVs at both observing bands. The project was divided into four observing campaigns, scheduled from November 2013 to September 2017. Table 1 lists the GMRT campaign ID, the allocated time, and the year(s) of completion.

Details of the targeted areas and observing parameters are given in Table 2: the name of the FoV, the corresponding campaign ID, the exact observation date, the position of the pointing center, the time on the FoVs (t.o.s.), the band, and the calibrators, ordered by band and by right ascension. The observations were carried out using the total intensity mode and a bandwidth of 32 MHz and 256 spectral channels to minimize the effect of bandwidth smearing. Flux calibrators were observed at the start and end of the each run for flux and bandpass calibration. A phase calibrator was observed for 5 min after a scan of 30 min on the target to calibrate the phases and any slow variations of the telescope gain.

4. Data reduction

The five pointings at 325 MHz were processed uniformly, using the SPAM routines (Intema 2014), which is a python package based on the Astronomical Image Processing System (AIPS) for nearly automatic analysis of GMRT data below 1 GHz. Bad data and RFI were initially flagged at the full spectral resolution of 256 channels. The flux was calibrated using the primary calibrators 3C286, 3C48, and 3C147 and the scale by Scaife & Heald (2012) for low radio frequencies. The SPAM pipeline then converted the precalibrated visibility data to a final image, which includes several rounds of self-calibration and flagging iteratively, and wide-field imaging to correct for noncoplanarity. In the self-calibration, ionospheric phase corrections were computed for several directions within the FoV for direction-dependent corrections on the integration timescales. The self-calibration procedure was followed using default parameters of SPAM, with initial cycles in phase with long intervals and a last run with the solution interval of the visibility integration time; in our case, 16.9 seconds. Toward the end of the loop, one round of amplitude and phase self-calibration was carried out. During imaging, a moderately uniform weighting scheme (robust = −1 in AIPS) was used, but no multiscale cleaning options were incorporated. Primary-beam corrections were applied using the GMRT specific parameters (GMRT Observer's Manual).

Because the target is in the Galactic plane, the $T_{\rm sys}$ correction for excess background was applied using the 408 MHz all-sky map (Haslam et al. 1982) during the calibration as part of the pipeline. The correction factor varied from 1.7 to 3.6, with the highest correction factor near the Galactic plane and a lower correction factor away from the plane. The FoVs were combined in a mosaic with weights as inverse of the variance.

The data analysis of the 47 FoVs at 610 MHz was also carried out using the SPAM pipeline, similar to the 325 MHz data. The $T_{\rm sys}$ correction for the excess background at 610 MHz ranged from 1.22 to 1.76. Fields of view FoV610.21 and FoV610.30 were noisier than the rest, probably because of strong extended emission from the Galactic plane and bright sources in the fields.

The final mosaics presented an average rms of 0.5 mJy beam^{-1} and 0.2 mJy beam^{-1} at 325 and 610 MHz, respectively, although locally, the values strongly depend mainly on the extended and/or diffuse emission. The synthesized beams attained were $10'' \times 10''$, and $6'' \times 6''$, and the mosaic image sizes were (6487×6573), and (12580×13837) pixels, respectively. The final images are presented in Figs. 3 and 4.

A series of factors affect the accuracy of low-frequency radio flux scales in different ways. This in turn affects the uncertainties. In their observations with the GMRT, Chandra et al. (2004), for instance, discussed a flux-scale uncertainty at 325 and 610 MHz of a few percent. In addition, when the target fields lie in the Galactic plane, as the field we present, the fact that $T_{\rm sys}$ can be significantly higher because the sky temperature is higher than toward the calibrator imposes an additional correction factor; although the SPAM pipeline estimates this factor, it is based in some assumptions and extrapolations that may introduce some inaccuracy. We used different flux calibrators, the primary-beam model is not perfect, and mosaicking different pointings into the final images we used for source extraction can all affect the flux scale. When all of this is taken into account, a very conservative approach is to adopt flux density uncertainties of 10%.

5. Source extraction

When the mosaics at the two observing bands were built, we searched for errors in the astrometry, first, by taking point sources in the entire two images into consideration. We did not find significant errors at the smaller pixel scale, which means that

Table 2. Observing runs and fields of view information.

Field of view	Campaign	Observing	Pointing center (J2000)		t.o.s.	Band	Calibrators
name	ID	dates	RA (h, m, s)	Dec (deg,′,″)	(min)	(MHz)	
FoV325.1	27_036	7/2,26/9/15	20 18 26	41 16 50	488	325	3C48,2052+365
FoV325.2	27_036	26/10/14	20 25 38	41 16 50	304	325	3C48,2052+365
FoV325.3	27_036	27/10/14	20 25 38	42 39 50	296	325	3C147,2052+365
FoV325.4	27_036	6/2/15	20 25 38	44 02 50	283	325	3C48,2052+365
FoV325.5	25_026	4/11/13	20 32 50	41 16 50	523	325	3C48,2038+513
FoV610.1	28_081	18/6/15	20 13 50	41 21 15	79	610	3C48,2052+365
FoV610.2	28_081	18/6/15	20 13 60	40 43 10	79	610	3C48,2052+365
FoV610.3	30_027	11,21/8/16	20 14 13	42 02 30	118	610	3C48,3C286,2052+365
FoV610.4	28_081	18/6/15	20 16 50	41 03 15	130	610	3C48,2052+365
FoV610.5	28_081	25/7/15	20 16 50	41 41 20	119	610	3C48,2052+365
FoV610.6	30_027	2/9/17	20 16 50	42 20 30	69	610	3C48,2052+365
FoV610.7	28_081	25/7/15	20 17 00	40 25 05	71	610	3C48,2052+365
FoV610.8	30_027	17/7,8/8/16	20 19 40	42 40 01	147	610	3C48,2052+365
FoV610.9	30_027	17/7,8/8/16	20 19 40	43 18 01	179	610	3C48,2052+365
FoV610.10	30_027	17/7/16	20 19 40	43 56 56	78	610	3C48,2052+365
FoV610.11	30_027	1/7/16	20 19 42	42 01 08	94	610	3C286,2052+365
FoV610.12	28_081	25/7/15	20 19 45	41 22 60	119	610	3C48,2052+365
FoV610.13	28_081	15/8/15	20 19 50	40 44 50	119	610	3C48,2052+365
FoV610.14	30_027	15/7/16	20 22 25	44 52 09	64	610	3C48,2052+365
FoV610.15	28_081	16/8/15	20 22 30	41 42 30	119	610	3C48,2052+365
FoV610.16	30_027	2/9/17	20 22 34	44 15 01	59	610	3C48,2052+365
FoV610.17	30_027	2/9/17	20 22 36	43 36 53	59	610	3C48,2052+365
FoV610.18	28_081	15/8/15	20 22 40	41 04 20	107	610	3C48,2052+365
FoV610.19	30_027	30/6,23/7/16	20 22 40	42 20 30	168	610	3C48,3C286,2052+365
FoV610.20	30_027	30/6,23/7/16	20 22 40	42 58 30	231	610	3C48,3C286,2052+365
FoV610.21	28_081	15/8/15	20 22 45	40 26 15	62	610	3C48,2052+365
FoV610.22	30_027	15/7/16	20 25 27	45 10 21	71	610	3C48,2052+365
FoV610.23	30_027	2/9/17	20 25 38	43 56 06	76	610	3C48,2052+365
FoV610.24	30_027	2/9/17	20 25 38	44 34 14	70	610	3C48,2052+365
FoV610.25	28_081	16/8/15	20 25 40	40 45 25	119	610	3C48,2052+365
FoV610.26	28_081	17/8/15	20 25 40	41 23 35	142	610	3C48,2052+365
FoV610.27	30_027	14/7/16	20 25 40	42 01 60	89	610	3C48,2052+365
FoV610.28	30_027	30/6,23/7/16	20 25 40	42 40 00	168	610	3C48,3C286,2052+365
FoV610.29	30_027	1,2,24/7/16	20 25 40	43 18 00	243	610	3C48,3C286,2052+365
FoV610.30	28_081	17/8/15	20 28 30	40 26 15	79	610	3C48,2052+365
FoV610.31	28_081	16/8/15	20 28 30	41 04 20	71	610	3C48,2052+365
FoV610.32	28_081	17/8/15	20 28 35	41 42 30	79	610	3C48,2052+365
FoV610.33	30_027	1,2,24/7/16	20 28 40	42 21 00	232	610	3C48,3C286,2052+365
FoV610.34	30_027	1,2,24/7/16	20 28 40	42 59 00	230	610	3C48,3C286,2052+365
FoV610.35	30_027	1/7/16	20 28 40	43 36 53	94	610	3C286, 2052+365
FoV610.36	30_027	1/7/16	20 28 42	44 15 01	94	610	3C286, 2052+365
FoV610.37	30_027	15/7/16	20 28 44	44 47 32	71	610	3C48, 2052+365
FoV610.38	27_036	28,29/11/14	20 29 55	40 57 38	120	610	3C48,2052+365
FoV610.39	27_036	28,29/11/14	20 29 55	41 35 45	120	610	3C48,2052+365
FoV610.40	30_027	17/7,8/8/16	20 31 45	42 21 39	145	610	3C48,2052+365
FoV610.41	27_036	28,29/11/14	20 32 50	40 38 42	120	610	3C48,2052+365
FoV610.42	30_027	14/7,8/8/16	20 32 50	41 16 50	165	610	3C48,2052+365
FoV610.43	27_036	28,29/11/14	20 32 50	41 54 58	120	610	3C48,2052+365
FoV610.44	27_036	28,29/11/14	20 35 45	40 57 38	105	610	3C48,2052+365
FoV610.45	27_036	28,29/11/14	20 35 45	41 35 45	120	610	3C48,2052+365
FoV610.46	30_027	8,11,21/8/16	20 36 17	40 22 30	177	610	3C48,3C286,2052+365
FoV610.47	30_027	11,21/8/16	20 36 17	42 16 30	118	610	3C48,3C286,2052+365

the accuracy was better than 1.5 arcsec. We also searched the 610 MHz image and point sources with well-determined optical positions, that is, Wolf-Rayet and O-type stars. For the cases with radio emission at or near the position of these stars (13 in total), the differences in coordinates were in the range 0.1–3.1″, and the standard deviation was 1.34″ (see Benaglia et al. 2020, for a study of the massive early-type stars detected in the current databases).

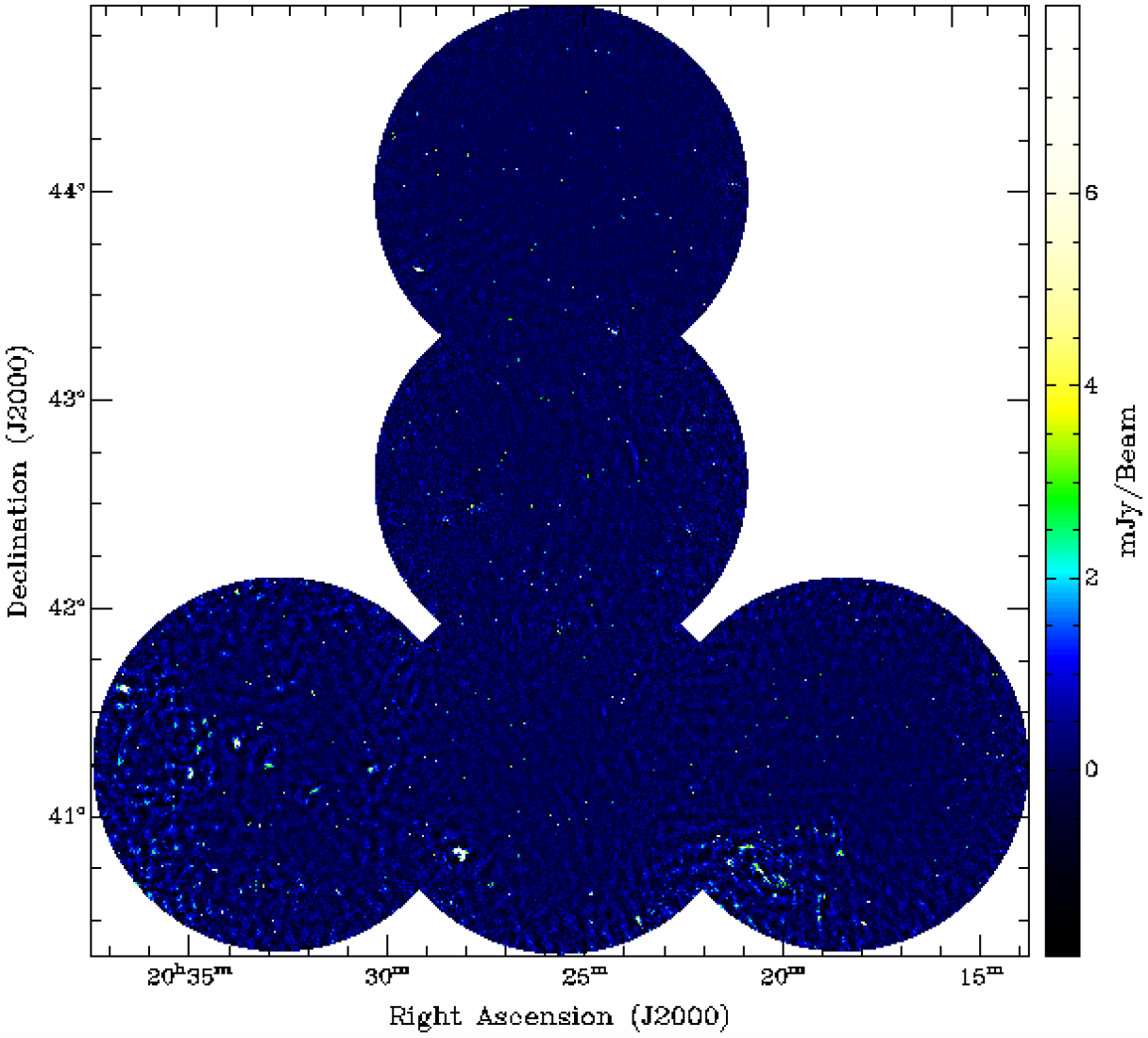

Fig. 3. GMRT 325 MHz continuum image of the observed field. The synthesized beam is $10'' \times 10''$, and the average rms is 0.5 mJy beam^{-1}. The full range of the flux density values is −9.2, +812.5 mJy beam^{-1}. The interval shown is (−2, +8) mJy beam^{-1} to outline the weaker features.

To survey the emission in the 325 and 610 MHz images, we applied the Python blob detector and source finder (PyBDSF[4]). The tool can be used to find islands of emission in radio interferometry images, decompose them into Gaussian functions, and finally gather them into individual source fits. We chose a signal-to-noise ratio of 7 as the lower limit for a source or fit to be accepted, and proceeded in the same way as Benaglia et al. (2019), where this proved successful. A similar detection threshold was used for the CORNISH catalog (Purcell et al. 2013). The routine includes the determination of the rms in the image and the production of a corresponding rms image.

The running of PyBDSF over the 325 and 610 MHz image mosaics resulted in 1230 and 3023 sources, respectively. After a thorough visual inspection of each source, we kept 1048 (85.2%) sources from the 325 MHz image and 2796 (92.5%) sources from the 610 MHz image.

The group of accepted entries consisted of discrete (unresolved) objects that were represented by one fitted source of the size of the synthesized beam, and of resolved objects. Some resolved objects were represented by a fitted source that was larger than the synthesized beam, while others were described by a combination of fitted sources.

We rejected fits to filaments and (part of) diffuse emission (3.5% at 325 MHz and 1.5% at 610 MHz, see Fig. 5a) and the fit combinations that corresponded to strong and/or large objects with ill representations (1.7% at 325 MHz and 2.0% at 610 MHz; Fig. 5b). We also discarded either objects with reduction artifacts that precluded a proper fit (including end-of-field objects: 2.5% at 325 MHz and 8.2% at 610 MHz, Fig. 5c) and fitted sources similar to surrounding noise (1.5% at 325 MHz and 1.3% at 610 MHz, see Fig. 5d).

Overall, the 610 MHz emission was better imaged by the SPAM pipelines than the emission at the lower frequency band. The 325 MHz mosaic presented a higher percentage of extended emission-fitting problems. The largest detectable structure is $32'$ at the 325 MHz band and $17'$ at the 610 MHz band (GMRT User's Manual): the data presented here are biased against structures that are larger than that. The selection of the robust weighting of −1, a compromise between high angular resolution and signal-to-noise ratio, outlined discrete sources over diffuse emission.

The attained rms at the two bands, in addition to the intrinsic values contributed by the stellar sources under observation, are

[4] http://www.astron.nl/citt/pybdsf/

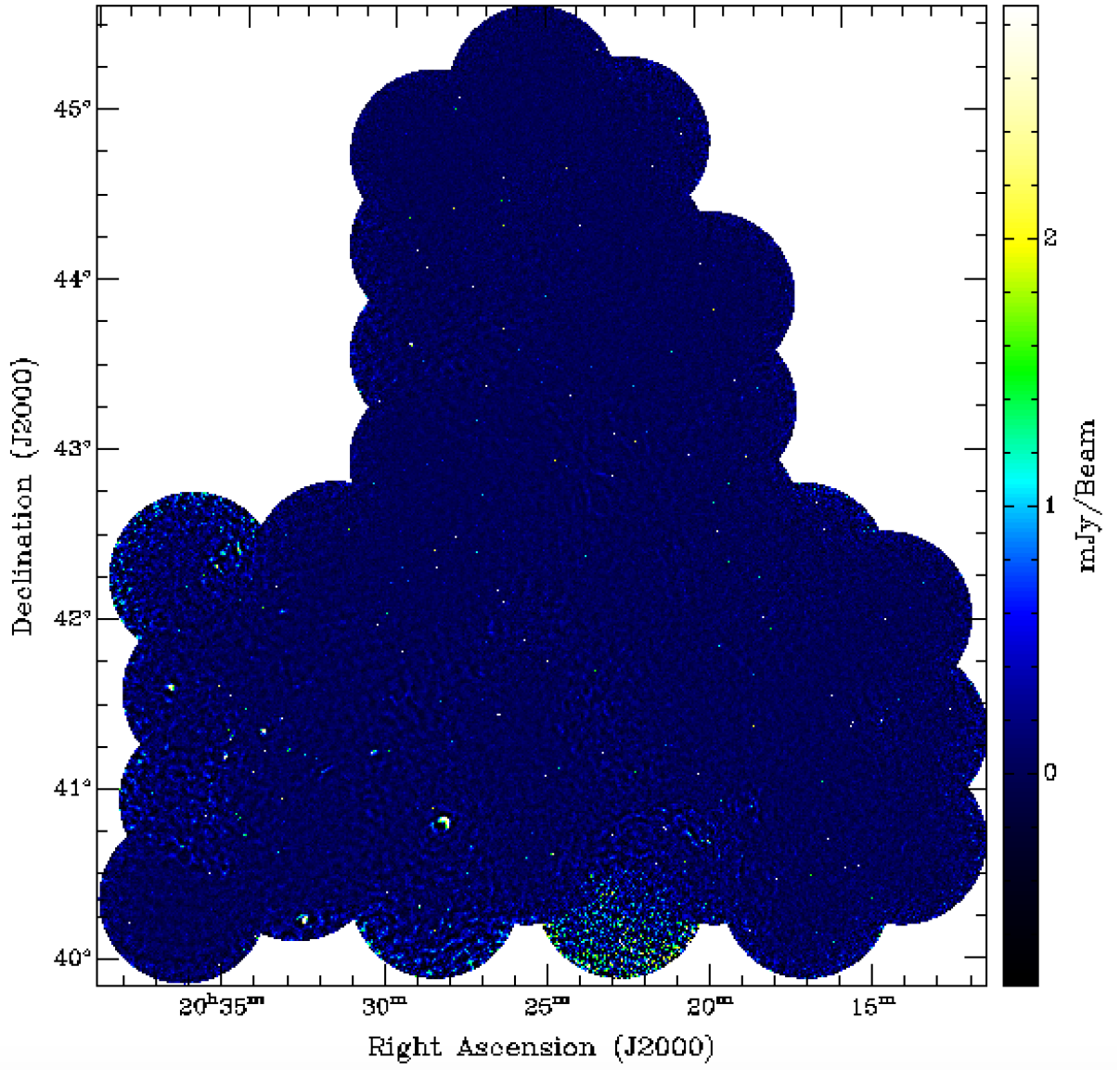

Fig. 4. GMRT 610 MHz continuum image of the observed field. The synthesized beam is $6'' \times 6''$, and the average rms is 0.2 mJy beam^{-1}. The full range of the flux density values is −6.3, +928.3 mJy beam^{-1}. The interval shown is (−0.8, +2.9) mJy beam^{-1} to outline the weaker features.

indeed a function of the time-on-source (here, time-on-fields). To determine the completeness of the sources detected above 7σ (7 rms), we also ran the PyBDSF routines using a detection threshold of 5σ. We found 1721 fitted sources at 325 MHz and 5015 at 610 MHz, which is well above the numbers found for the first run. When we visually inspected several faint sources, they appeared like noise peaks, which prompted us to use 7σ, with which we found significantly fewer spurious sources. The incompleteness of our catalog is mainly quantified by the reasons given above regarding the fits.

The final lists of the accepted objects are reunited in our catalog. The cataloged sources are given in Tables 3 and 4, named consecutively (Col. 1) by increasing right ascension; only sample items are shown. We tagged the sources with the label "BIC" followed by the observing frequency in MHz, and then a correlative number, based on their order. For each source, we list the coordinates RA, Dec (J2000) of the fit (Cols. 2 and 3), the integrated flux (Col. 4), the peak flux (Col. 5) and the fitted major axis, minor axis, and position angle (θ_1, θ_2, and PA, Cols. 6–8), which represent the source size and orientation after deconvolution, all with their corresponding errors as reported by PyBDSF. The full Tables 3 and 4 are provided at the CDS.

6. Determining spectral indices

The spectral index α of a source is a key parameter in the determination of its nature. When the flux densities at frequency bands centered at ν_1 and ν_2 are S_1 and S_2, and $S_\nu \propto \nu^\alpha$, $\alpha = \log(S_1/S_2)/\log(\nu_1/\nu_2)$. For the observations we processed, $\nu_1 = 325$ MHz and $\nu_2 = 610$ MHz, and α can be derived when a source was detected at both bands.

In the process of obtaining spectral index information, we verified whether the sources we detected at one of the observing bands were positionally coincident with one or more sources detected at the other band. To do this, we determined for each 325 MHz source ellipse whether it overlapped one or more of the 610 MHz source ellipses. When this was the case, we classified the overlapping as partial when the ellipse at 325 MHz partially overlapped the ellipse at 610 MHz, or as full when the 610 MHz

Table 3. Detected sources at 325 MHz above the 7σ level (first entries).

ID	RA_{J2000} (h, m, s)	Dec_{J2000} (deg,′,″)	Total flux (mJy)	Peak flux (mJy/beam)	θ_1 (″)	θ_2 (″)	PA (°)
BIC325-0001	20:13:54.55 ± 0.049	41:32:32.01 ± 0.88	4.7 ± 1.00	2.8 ± 0.40	13.9 ± 2.10	13.9 ± 2.10	16.0 ± 46.54
BIC325-0002	20:13:56.45 ± 0.025	41:33:06.07 ± 0.30	16.7 ± 1.19	7.7 ± 0.39	17.2 ± 0.97	17.2 ± 0.97	56.4 ± 6.23
BIC325-0003	20:14:04.78 ± 0.024	40:56:14.47 ± 0.27	5.1 ± 0.63	5.0 ± 0.36	10.8 ± 0.83	10.8 ± 0.83	93.3 ± 21.93
BIC325-0004	20:14:07.82 ± 0.037	41:02:47.35 ± 0.61	3.4 ± 0.69	2.8 ± 0.36	11.2 ± 1.44	11.2 ± 1.44	7.9 ± 87.95
BIC325-0005	20:14:17.56 ± 0.003	41:29:24.16 ± 0.03	80.9 ± 0.83	58.9 ± 0.38	12.9 ± 0.09	12.9 ± 0.09	77.2 ± 179.64
BIC325-0006	20:14:18.62 ± 0.007	41:18:10.88 ± 0.07	43.3 ± 0.97	25.0 ± 0.38	14.5 ± 0.24	14.5 ± 0.24	74.8 ± 1.70
BIC325-0007	20:14:19.17 ± 0.003	41:29:36.95 ± 0.04	54.7 ± 0.79	42.2 ± 0.38	12.0 ± 0.11	12.0 ± 0.11	73.0 ± 1.59
BIC325-0008	20:14:24.35 ± 0.012	41:41:32.07 ± 0.36	24.3 ± 1.48	10.4 ± 0.38	18.5 ± 0.91	18.5 ± 0.91	110.5 ± 3.29
BIC325-0009	20:14:27.13 ± 0.036	41:17:52.59 ± 0.36	6.5 ± 0.85	4.4 ± 0.37	13.7 ± 1.28	13.7 ± 1.28	76.4 ± 14.16
BIC325-0010	20:14:29.42 ± 0.014	41:41:32.46 ± 0.13	24.1 ± 1.04	14.0 ± 0.41	15.4 ± 0.51	15.4 ± 0.51	81.4 ± 2.61

Notes. θ_1, θ_2, and PA represent the elliptic source size and orientation, and correspond to the major axis, the minor axis, and the position angle of the fit by the PyBDSM routines. The full table with 1048 records is available at the CDS.

Table 4. Detected sources at 610 MHz above the 7σ level (first entries).

ID	RA_{J2000} (h, m, s)	Dec_{J2000} (deg,′,″)	Total flux (mJy)	Peak flux (mJy/beam)	θ_1 (″)	θ_2 (″)	PA (°)
BIC610-0001	20:11:32.02 ± 0.009	40:53:10.84 ± 0.10	14.5 ± 0.69	7.8 ± 0.26	9.3 ± 0.34	9.3 ± 0.34	63.3 ± 3.83
BIC610-0002	20:11:33.03 ± 0.001	40:53:18.92 ± 0.02	63.8 ± 0.75	42.0 ± 0.24	7.9 ± 0.06	7.9 ± 0.06	60.6 ± 1.35
BIC610-0003	20:11:34.94 ± 0.009	41:31:49.27 ± 0.09	12.5 ± 0.63	7.9 ± 0.26	8.8 ± 0.33	8.8 ± 0.33	112.7 ± 2.90
BIC610-0004	20:11:48.15 ± 0.019	40:51:32.52 ± 0.25	2.3 ± 0.40	2.3 ± 0.23	6.6 ± 0.73	6.6 ± 0.73	53.2 ± 23.77
BIC610-0005	20:11:53.58 ± 0.007	40:48:39.49 ± 0.11	8.6 ± 0.50	6.4 ± 0.24	7.4 ± 0.29	7.4 ± 0.29	128.0 ± 11.67
BIC610-0006	20:11:55.45 ± 0.008	42:13:40.96 ± 0.11	4.3 ± 0.33	4.1 ± 0.19	6.3 ± 0.30	6.3 ± 0.30	106.9 ± 27.75
BIC610-0007	20:11:56.63 ± 0.014	42:13:37.89 ± 0.24	2.4 ± 0.34	2.2 ± 0.19	6.7 ± 0.60	6.7 ± 0.60	142.6 ± 23.84
BIC610-0008	20:11:58.89 ± 0.009	41:47:49.24 ± 0.18	2.0 ± 0.27	2.6 ± 0.18	5.6 ± 0.42	5.6 ± 0.42	1.1 ± 21.54
BIC610-0009	20:11:59.38 ± 0.007	40:28:25.33 ± 0.09	7.6 ± 0.44	6.7 ± 0.23	6.8 ± 0.25	6.8 ± 0.25	57.4 ± 11.20
BIC610-0010	20:12:00.79 ± 0.018	42:02:34.40 ± 0.28	2.1 ± 0.34	1.8 ± 0.17	6.7 ± 0.69	6.7 ± 0.69	134.7 ± 70.97

Notes. θ_1, θ_2, and PA represent the elliptic source size and orientation, and correspond to the major axis, the minor axis, and the position angle of the fit by the PyBDSM routines. The full table with 2796 records is available at the CDS.

Table 5. Sources detected at both frequency bands (325 and 610 MHz) and spectral index information (first entries).

ID at 325 MHz	RA, Dec_{J2000} (hms, dms)	ID at 610 MHz	$\alpha^{325\,MHz}_{610\,MHz}$
BIC325-0002	20:13:56.45, 41:33:06.07	BIC610-0104, −0105	−0.4 ± 0.26
BIC325-0003	20:14:04.78, 40:56:14.47	BIC610-0109	−0.7 ± 0.32
BIC325-0004	20:14:07.82, 41:02:47.35	BIC610-0112	−1.4 ± 0.48
BIC325-0005	20:14:17.56, 41:29:24.16	BIC610-0123	−1.1 ± 0.23
BIC325-0006	20:14:18.62, 41:18:10.88	BIC610-0124	−1.0 ± 0.23
BIC325-0007	20:14:19.17, 41:29:36.95	BIC610-0126	−0.9 ± 0.23
BIC325-0008	20:14:24.35, 41:41:32.07	BIC610-0133, −0134, −0131	−0.8 ± 0.25
BIC325-0009	20:14:27.13, 41:17:52.59	BIC610-0140	−1.2 ± 0.34
BIC325-0010	20:14:29.42, 41:41:32.46	BIC610-0146	−1.3 ± 0.24
BIC325-0012	20:14:30.76 , 41:41:41.64	BIC610-0147	−0.9 ± 0.25

Notes. The full table of 993 records is available at the CDS.

ellipse was contained in the 325 MHz ellipse. For partial cases, we registered the percentage of overlapping area (OA).

We then studied the 610 MHz ellipse/s that was/were related to each single 325 MHz ellipses and calculated a corresponding 610 MHz contributing flux SC_2 that we used in the spectral index expression in the following way. For full cases, we considered $SC_2 = S_2$. For partial cases, we set $SC_2 = S_2$ when $OA \geq 70\%$, $SC_2 = 0.5\,S_2$ when $70\% > OA > 30\%$, and $SC_2 = 0$ elsewhere. We found that 993 sources at 325 MHz overlap one or more 610 MHz sources, and we computed the corresponding spectral indices by considering for each source at 325 MHz all the overlapping sources at 610 MHz with the weights as explained above. Table 5 lists the 325 MHz source with its central coordinates, the 610 MHz source(s) that partially or fully overlap the former, and the spectral index α as derived from S_1 and SC_2 (a few entries; the full table is available at the

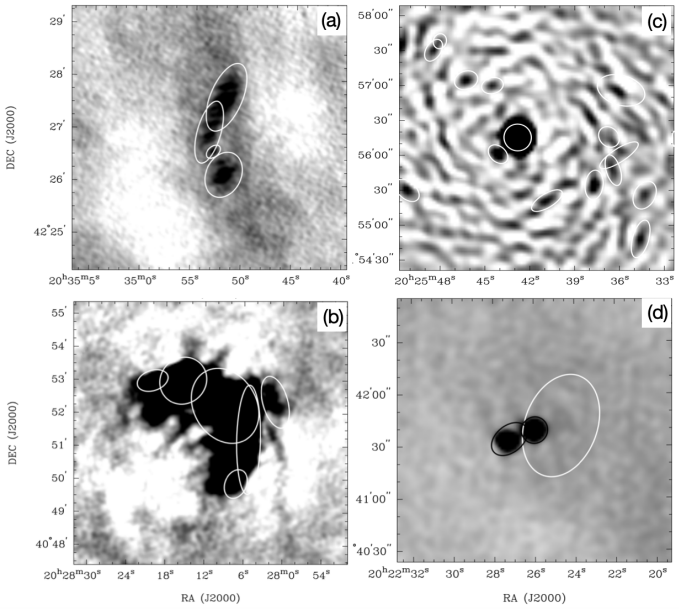

Fig. 5. Examples of discarded fits for the four cases given in Sect. 5, represented as white-line ellipses. (*a*): Filaments and/or diffuse emission at 610 MHz. (*b*): Strong or large sources that are ill represented by a combination of fits at 325 MHz. (*c*): Reduction artifacts at 325 MHz. (*d*): Fits of emission similar to the noise at 610 MHz; in this last case, the fits accepted as good fits are shown with black-line ellipses.

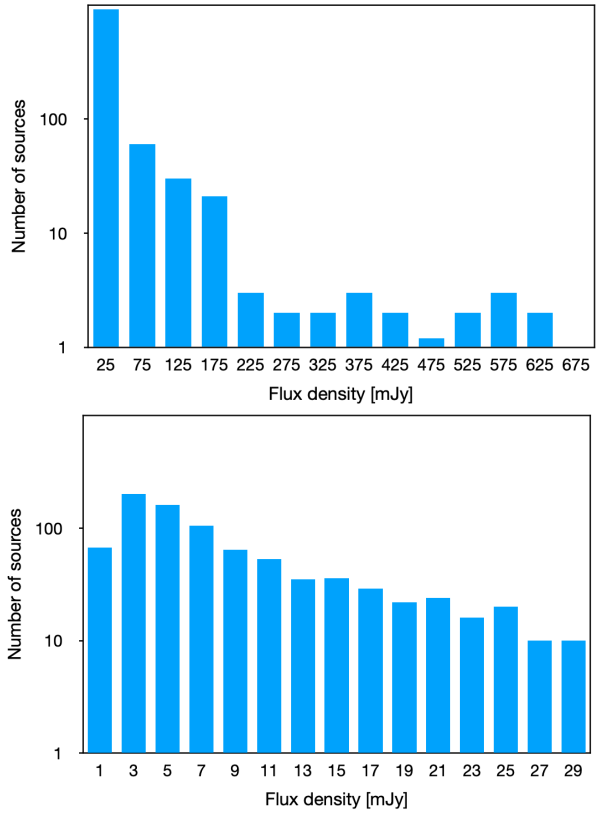

Fig. 6. *Top*: number of sources as a function of their integrated flux density for 99.71% of the sources cataloged at 325 MHz. *Bottom*: same for flux densities up to 30 mJy (841 sources out of 1048, i.e., 80%).

CDS). We present the spectral index uncertainty by error propagation in the very conservative case, that is, using the flux density errors given by PyBDSF combined with a 10% error for flux density scales (see Sect. 4).

To evaluate the probability of random matches when spectral indices are derived, we calculated the inverse of the number of sources per square degree over the area of the synthesized beam. At 325 MHz, we obtained that there will be one such a coincidence in 1700 sources. At 610 MHz, the probability of a random match is one source in 3230. We found 1048 sources at 325 MHz, and 2796 sources at 610 MHz, therefore we assume that is very unlikely that unrelated sources overlap in our sample.

7. Catalog properties

7.1. Detections, flux densities, and noise levels

The catalog comprises 1048 sources at 325 MHz and 2796 sources at 610 MHz with flux densities greater than 7σ; here σ represents the local rms noise at the source surroundings. The sources are characterized by their integrated and peak flux densities with corresponding errors, major and minor axes, and the position angle of a fitted ellipse, also with their errors.

Figure 6 displays the distribution of the flux density of the sources detected at the 325 MHz band. In the lower panel we present a zoom on the flux interval 0–30 mJy, which contains 80% of the sources. The corresponding histograms for 610 MHz appear in Fig. 7, with 91% of the sources with fluxes up to 30 mJy. At both bands, the effect of favoring higher resolution (meanwhile outlining more discrete sources) by means of the weighting scheme is appreciable as a majority of sources with lower fluxes. The detail for the sources with lower flux shows the typical decrease with flux (see, e.g., Fig. 3 in Zoonematkermani et al. 1990). The lower number of sources up to 5 mJy at 325 MHz is probably the effect of the detection threshold at this band (≃2 mJy on average).

We compared the number of sources we detected with the results from other studies. At the 325 MHz band, the survey by Taylor et al. (1996), carried out with the Westerbork Synthesis Radio Telescope (WSRT) at 327 MHz, reported 3984 sources over a detection threshold of 10 mJy, an area of 160 sq deg, and an angular resolution ≥1′, which means a ratio R of 24.9 sources per square degree. At a similar frequency, we obtained 453 sources with fluxes above 10 mJy, thus a ratio of 40.1 sources per square degree. The difference can be explained by the larger beam that was used by the former survey, which is six times larger than the synthesised beam we used because some nearby GMRT sources will be seen as one WSRT source. A quick comparison with the detections reported by Setia Gunawan et al. (2003) (synthezised beam larger than five times that of this research) found that more than 90% of their sources that are present in the area are in common.

The VLA FIRST survey (Becker et al. 1995), performed at 20 cm, found 946432 sources above a detection threshold of 1 mJy (0.15 mJy rms) using angular resolution images of ∼5″ over an area of 10575 sq deg, and then R = 89.5. The FIRST detection limit corresponds to a value of 1.8 mJy when it is scaled to the 610 MHz band using a spectral index of −0.7. In our catalog, almost 1800 sources showed flux densities higher than 1.8 mJy and R = 91.4, which agrees very well with the results from Becker et al. (1995).

For the rms per pixel at each band, we present in Fig. 8 the histograms showing the distribution of the rms in the fields we observed as obtained when the PyBDSF routines were applied at both bands. This rms value is estimated by PyBDSF near each

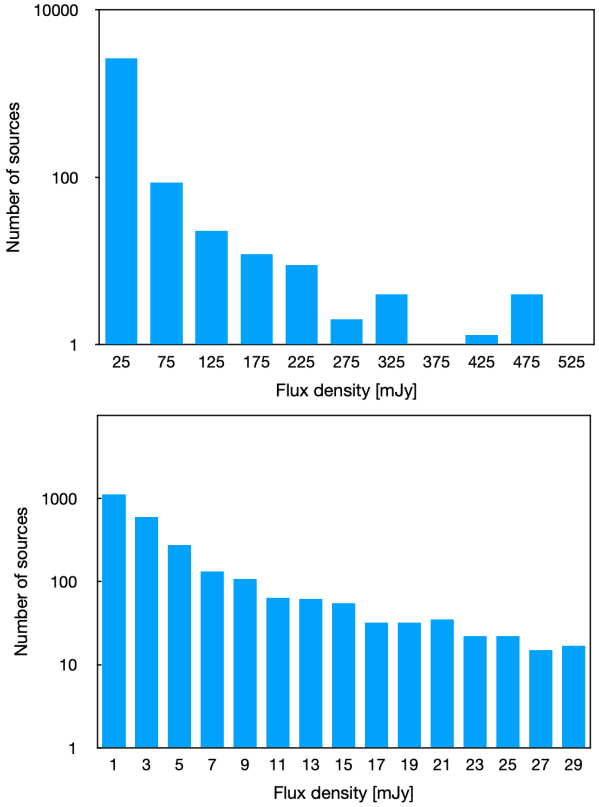

Fig. 7. *Top*: number of sources as a function of their integrated flux density for 99.75% of the sources cataloged at 610 MHz. *Bottom*: same for flux densities up to 30 mJy (2565 sources out of 2796, i.e., 91%).

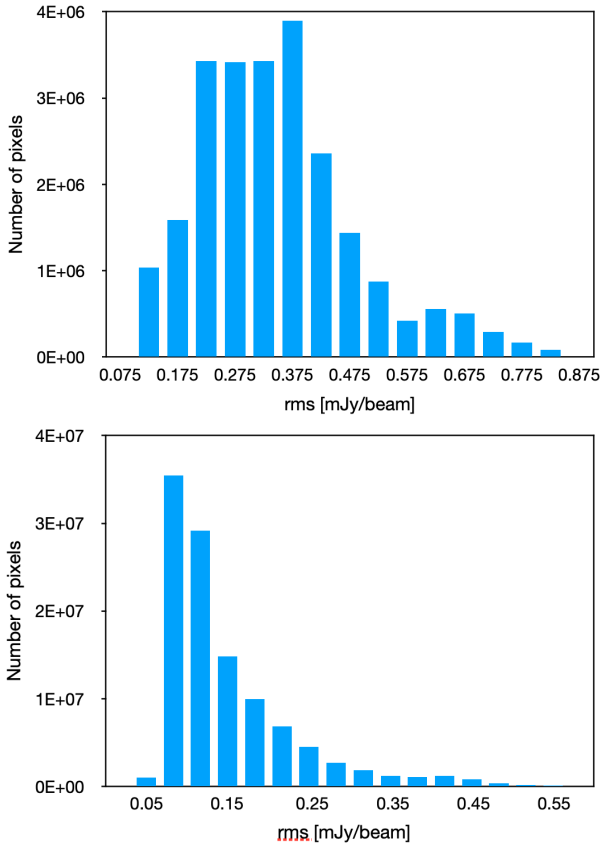

Fig. 8. Distribution of the rms in the mosaics at 325 MHz (*top panel*) and at 610 MHz (*bottom panel*).

source before fitting. At 325 MHz, 88% of the pixels show an rms of up to 0.5 mJy beam^{-1}. At 610 MHz, 80% of the pixels show an rms of up to 0.2 mJy beam^{-1}. We also compared these rms values and the rms values of a residual image from which the contribution of the fitted sources was subtracted. The results are presented in Fig. 9. The rms values decrease considerably, as expected.

7.2. Resolved and unresolved sources

To distinguish between resolved and unresolved sources, we plot in Fig. 10 the ratio of the total (integrated) flux over the peak flux for circular sources ($\theta_1/\theta_2 < 1.05$, 418 sources) at 610 MHz. The ratio remains below 1.25 out to 6.6″, which we adopt as the dividing line between resolved and unresolved sources. This value by coincidence is the size of the synthesised beam plus a 10% error at this frequency. We applied the same criterion based on the ratio value of 1.25 for the sources detected at 325 MHz. The distribution of the mean axes (sizes) of the cataloged sources, in the form of the average of the major and minor axes of each ellipse, is shown in Figs. 11 and 12.

7.3. Source multiplicity

During the visual inspection process of all sources we found at both bands, we marked those that are characterized by adjacent emission components, fit by distinct Gaussian functions. In many of them, even a bridge linking components was clearly seen. Following the technique by Magliocchetti et al. (1998) and Huynh et al. (2005), we listed the sources that presented a companion up to 2′, and distinguished the pairs (source+companion) where the flux density ratio (brighter over weaker) remained

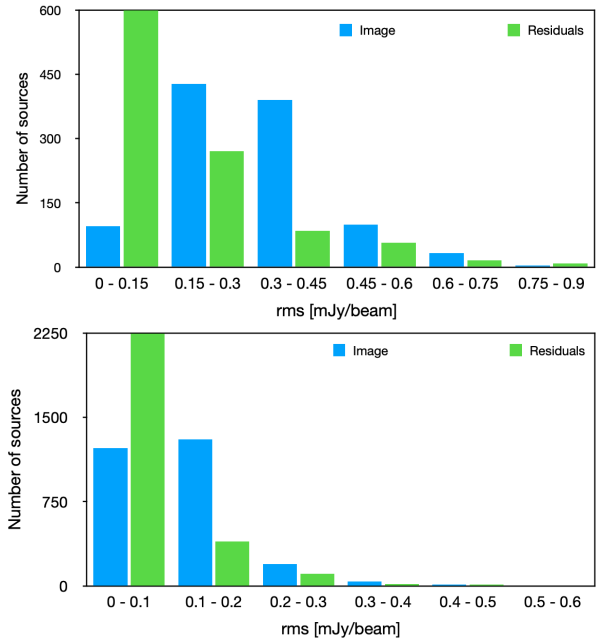

Fig. 9. Distribution of the rms in the mosaics before (light blue bars) and after source extraction (green bars) at 325 MHz (*top panel*) and at 610 MHz (*bottom panel*).

below 4. Figure 13 represents these groups in the plane of the sum of the fluxes (FS) of the components for each pair versus the separation (x) between components.

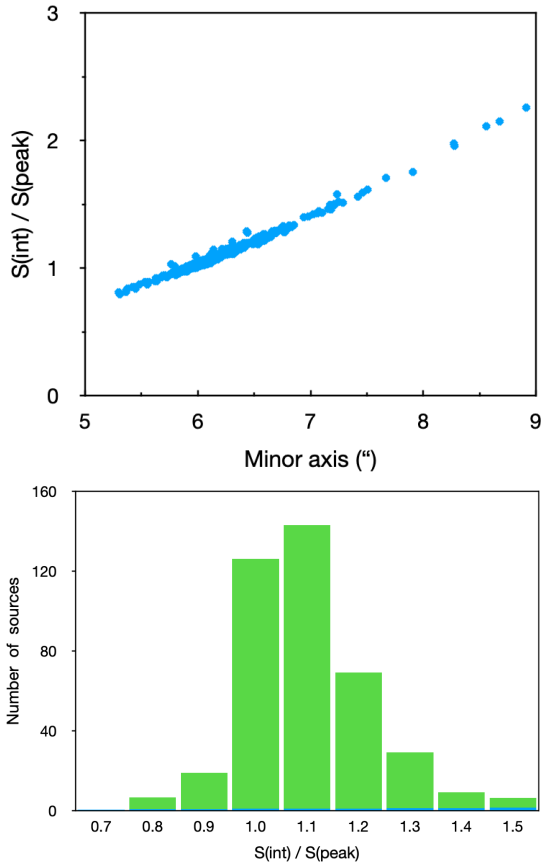

Fig. 10. *Top panel*: ratio of total flux over peak flux as a function of their minor axis for sources with $\theta_1/\theta_2 \leq 1.05$, cataloged at 610 MHz. A power fit yields $S_{\rm int}/S_{\rm peak} = 1.25$ at $\theta_2 = 6.6''$. *Bottom panel*: distribution of the flux ratio of the same group of sources.

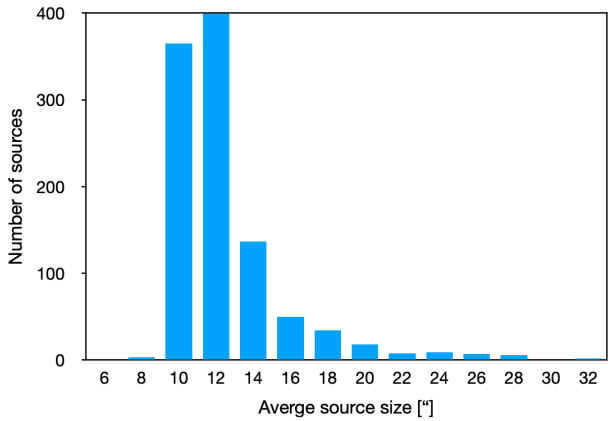

Fig. 11. Distribution of the average axis [0.5 × (major axis + minor axis)] of the ellipses representing the sources at 325 MHz.

Two areas are clearly visible in the plots at both bands, depending on whether they contain visually checked double pairs. Previous works have found that the limit between the areas can be described by $FS \propto x^2$. The data presented here appear to be better confined with an exponential of 3.5; see Fig. 13, where we plot the two limiting lines. In principle, we can infer that the components of the pairs in the left areas are more likely to be physically related.

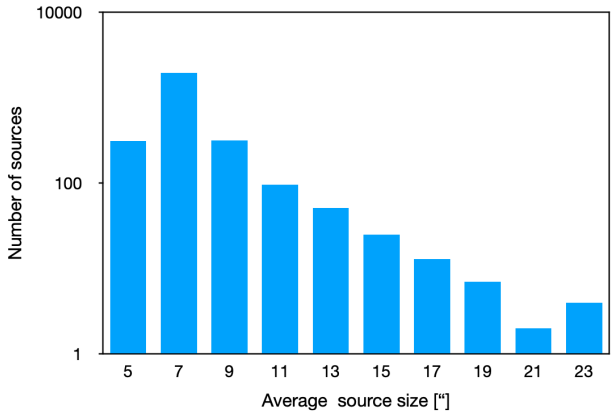

Fig. 12. Distribution of the average axis [0.5 × (major axis + minor axis)] of the ellipses representing the sources at 610 MHz.

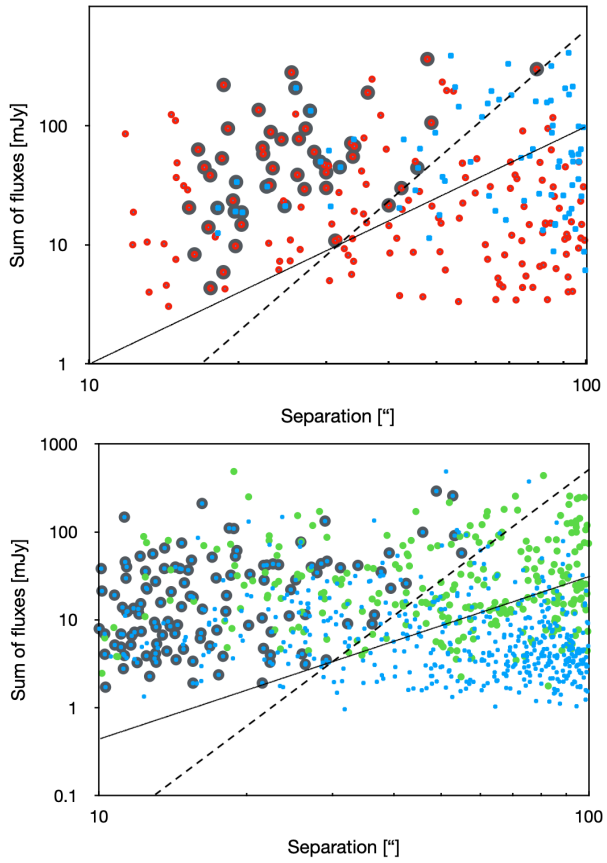

Fig. 13. Sum of the flux densities from pairs of nearby sources (FS) vs. source separation (x). *Top panel*: 325 MHz sources; in red, pairs of sources whose flux ratio (integrated/peak) is below 4; in blue, the rest; larger dark gray circles: pairs of confirmed double sources (see text). Dashed line: $(x/16)^{3.5}$. Thin solid line: $(x/10)^2$. *Bottom panel*: for 610 MHz sources; in green, pairs of sources whose flux ratio is below 4; in blue, the rest; larger dark gray circles: pairs of double sources (see text). Dashed line: $(x/20)^{3.5}$. Thin solid line: $(x/16)^2$.

7.4. Considerations of the spectral indices

In the case of the spectral index distribution of the about one thousand sources that are detected at two bands in our catalog, the pronounced maximum at $\alpha = -1$ confirms the nonthermal nature of most of the sources, see Figs. 14 and 15. The median error in α is 0.29. The spectral index values span from −3.06

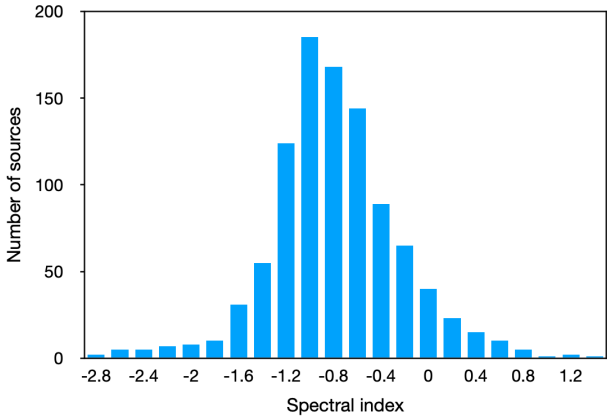

Fig. 14. Distribution of spectral indices corresponding to the sources detected at both frequency bands (see Table 5).

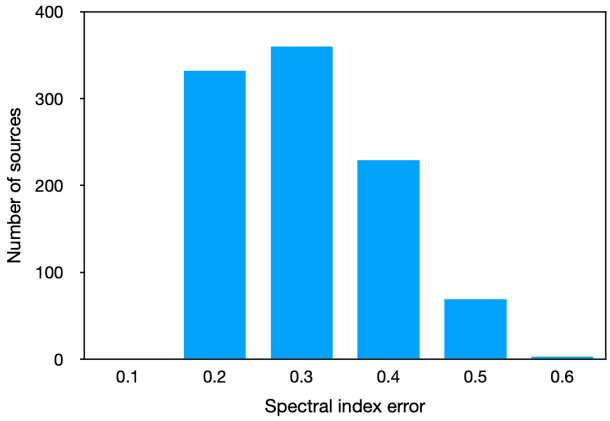

Fig. 15. Distribution of spectral index errors corresponding to the sources detected at both frequency bands (see Table 5).

to +1.41. Only 4 out of 993 values are below −2.5. Variability can be one of the reasons for the extreme absolute values of the index: the two frequency data were taken at different times. They might also arise because we systematically considered the fluxes for sources that do not fully overlap.

The uncertainties on the spectral indices are somewhat large, which is due to the conservative error on the flux density and because the two frequencies lie only about a factor of two apart. However, this should be sufficient to broadly categorize the sources as thermal, nonthermal, or pick up sources with very steep spectra.

The 993 sources with a spectral index value detected at the 325 MHz band correspond to 1065 sources at the 610 MHz band: at this latter frequency, the synthesized beam is smaller, and we found two or even three 610 MHz sources that overlap the same 325 MHz object; see Table 5. The surveyed area at 325 MHz totaled 23486672 pixels with signal (pixel size = 2.5″ × 2.5″), or 11.3 sq deg. At 610 MHz, 113370869 pixels with signal accounted for 19.7 sq deg (pixel size = 1.5″ × 1.5″). In the same area covered by the 325 MHz mosaic, 1796 sources at 610 MHz (out of the total number of 2796) were fit, thus the ratio of source-fits at 610 to 325 MHz is 1.71. This can be explained by sensitivity limitations, considering that at 610 MHz we have better angular resolution and lower noise, which allows us to detect thermal sources that will remain undetected at 325 MHz also because they are fainter, except for the cases when we picked up more than one source counterpart of a single 325 MHz source at 610 MHz.

8. Search for counterparts

After the catalog of 325 and 610 MHz sources was completed, we searched for nearby objects as possible counterparts to the (1048+2796=) 3844 entries. We used the Simbad database[5], with two input tables: one containing the coordinates of the records of the 325 MHz sources, and a second table with those of the 610 MHz sources. The search radius was set as the semi-major axis of the ellipse fit of each record. We found possible counterparts for 85 sources at 325 MHz and for 138 sources at 610 MHz, where more than one nearby object was found for some of the sources. We studied all possible counterparts in each case and also verified that the nearby objects were inside the fitted ellipse, that is, taking the semiminor axis and position angle of the source fit into consideration. We gathered the findings in Table A.1, which presents possible counterparts for 5 sources that are only detected at 325 MHz, for 52 sources that are only detected at 610 MHz, and for 86 sources that are detected at both bands, ordered by right ascension. The angular distance d between the GMRT source and the potential counterpart and the spectral index, if applicable, is also listed. By searching the literature, we investigated the nature of the potential counterpart, and propose the more plausible object that could be associated with the GMRT sources reported here whenever possible, along with its reference or, in the worst case, the reference of flux measured at other wavelength(s). In the cases with preexisting 325 MHz observations, we quote no counterpart because our observations superseded them in sensitivity or also in angular resolution. In addition to information from the surveys mentioned in Sect. 2, valuable material was found in Vollmer et al. (2010), who compiled flux values of sources at the radio range including those of the Cygnus region relevant here. An exception is made for fluxes at the 610 MHz band, for which no previous data were found. In this sense, our catalog completes many radio spectra and provides 610 MHz flux values of ∼2800 sources for the first time.

Of the sources with possible counterparts that were detected at both frequencies, 16% have flat or positive spectral index (nominally, $\alpha > -0.2$). Their counterparts are mostly either stars, young stellar objects, or radio sources detected at higher frequencies.

At the 325 MHz band, 8% of all the 325 MHz cataloged sources have a possible counterpart. At 610 MHz, 5% of all the 610 MHz cataloged sources have a possible counterpart. These low percentages can be explained considering that at the observed bands, decimeter wavelengths, we mostly sample nonthermal sources, at which high-energy (HE) processes presumably take place. These might be potential counterparts to the HE sources; but the angular resolutions and sensitivities for instruments working at HE ranges are higher and lower, respectively, precluding successful cross-identifications between radio and HE sources.

Preliminary results of a study focused on the unresolved unidentified sources with negative spectral index (∼340 sources of the present catalog), such as was performed by Chakraborty et al. (2020), indicated that differential source counts in the distribution trend of extragalactic sources result from other surveys or catalogs. However, we recall that the observed fields are in the surroundings of the Galactic plane, dense in Galactic sources, both of thermal and nonthermal nature. A detailed investigation to

[5] http://simbad.u-strasbg.fr/simbad/sim-fid

distinguish in which proportion, and more interesting, from which types of objects, Galactic and extragalactic sources contribute etc. is beyond the scope of this paper.

9. Related studies and prospects

The GMRT observations that gave rise to our catalog allowed us simultaneously to carry out research on individual populations of astronomical objects. Specifically, different types of objects that can produce nonthermal emission were or are being studied in separated investigations: AGNs and two-lobed sources, counterparts to HE sources, massive early-type stars (Benaglia et al. 2020), protoplanetary disk-like sources (Isequilla et al. 2019) and young stellar objects (Isequilla et al. 2020). Finally, the survey images will be presented elsewhere. Future work includes the scrutiny of sources between 3 and 7σ. The corresponding source extraction, after a thorough validation process, of such a large area with the angular resolution of a few arcseconds provided by the GMRT data at decimeter frequencies will certainly reveal a plethora of interesting objects and powerful statistical results of the nonthermal sky.

Acknowledgements. The authors are grateful to the referee, whose comments and suggestions resulted in improving the analysis and presentation of the article. The GMRT is operated by the National Centre for Radio Astrophysics of the Tata Institute of Fundamental Research. We thank the staff of the GMRT that made these observations possible. PB acknowledges support from ANPCyT PICT 0773–2017, and the contacts at NCRA, Pune for a very pleasant stay. ICCH acknowledges the support of the Department of Atomic Energy, Government of India, under the project 12-R&D-TFR-5.02-0700. This research has made use of the SIMBAD database, operated at CDS, Strasbourg, France, and of NASA's Astrophysics Data System bibliographic services.

References

Abeysekara, A. U., Archer, A., Aune, T., et al. 2018, ApJ, 861, 134
Albacete Colombo, J. F., Flaccomio, E., Micela, G., Sciortino, S., & Damiani, F. 2007, A&A, 464, 211
Anderson, L. D., Armentrout, W. P., Johnstone, B. M., et al. 2015, ApJS, 221, 26
Araudo, A. T., Romero, G. E., Bosch-Ramon, V., & Paredes, J. M. 2007, A&A, 476, 1289
Becker, R. H., White, R. L., & Helfand, D. J. 1995, ApJ, 450, 559
Benaglia, P., & Romero, G. E. 2003, A&A, 399, 1121
Benaglia, P., Romero, G. E., Martí, J., Peri, C. S., & Araudo, A. T. 2010, A&A, 517, L10
Benaglia, P., del Palacio, S., Ishwara-Chandra, C. H., et al. 2019, A&A, 625, A99
Benaglia, P., De Becker, M., Ishwara-Chandra, C. H., Intema, H., & Isequilla, N. 2020, PASA, 38, 1
Bosch-Ramon, V., Romero, G. E., Araudo, A. T., & Paredes, J. M. 2010, A&A, 511, A8
Brinkmann, W., Siebert, J., Feigelson, E. D., et al. 1997, A&A, 323, 739
Bulgarelli, A., Fioretti, V., Parmiggiani, N., et al. 2019, A&A, 627, A13
Chakraborty, A., Roy, N., Wang, Y., et al. 2020, MNRAS, 492, 2236
Chandra, P., Ray, A., & Bhatnagar, S. 2004, ApJ, 612, 974
Chen, A. M., Takata, J., Yi, S. X., Yu, Y. W., & Cheng, K. S. 2019, A&A, 627, A87
Clegg, A. W., Cordes, J. M., Simonetti, J. M., & Kulkarni, S. R. 1992, ApJ, 386, 143
Colley, D. 1980, MNRAS, 192, 377
Comerón, F., Pasquali, A., Rodighiero, G., et al. 2002, A&A, 389, 874
Condon, J. J., Cotton, W. D., Greisen, E. W., et al. 1998, AJ, 115, 1693
Cutri, R. M., Skrutskie, M. F., van Dyk, S., et al. 2003, VizieR Online Data Catalog, II/246
De Becker, M., & Raucq, F. 2013, A&A, 558, A28
del Palacio, S., Bosch-Ramon, V., Müller, A. L., & Romero, G. E. 2018, A&A, 617, A13
del Valle, M. V., & Pohl, M. 2018, ApJ, 864, 19
Douglas, J. N., Bash, F. N., Bozyan, F. A., Torrence, G. W., & Wolfe, C. 1996, AJ, 111, 1945
Elyajouri, M., Monreal-Ibero, A., Remy, Q., & Lallement, R. 2016, ApJS, 225, 19
Garwood, R. W., Perley, R. A., Dickey, J. M., & Murray, M. A. 1988, AJ, 96, 1655
Greaves, J. 2004, MNRAS, 355, 585
Hartman, R. C., Bertsch, D. L., Bloom, S. D., et al. 1999, ApJS, 123, 79
Haslam, C. G. T., Salter, C. J., Stoffel, H., & Wilson, W. E. 1982, A&AS, 47, 1
Hermsen, W., Swanenburg, B. N., Bignami, G. F., et al. 1977, Nature, 269, 494
Higgs, L. A., Wendker, H. J., & Landecker, T. L. 1994, A&A, 291, 295
Høg, E., Fabricius, C., Makarov, V. V., et al. 2000, A&A, 355, L27
Huynh, M. T., Jackson, C. A., Norris, R. P., & Prandoni, I. 2005, AJ, 130, 1373
Immer, K., Brunthaler, A., Reid, M. J., et al. 2011, ApJS, 194, 25
Intema, H. T. 2014, SPAM: Source Peeling and Atmospheric Modeling (Astrophysics Source Code Library)
Isequilla, N. L., Fernández-López, M., Benaglia, P., Ishwara-Chandra, C. H., & del Palacio, S. 2019, A&A, 627, A58
Isequilla, N. L., Benaglia, P., Ishwara-Chandra, C. H., & Intema, H. 2020, Bol. Asoc. Argent. Astron., 61B, 1
Ishwara-Chandra, C. H., Benaglia, P., De Becker, M., & Tej, A. 2019, Bull. Soc. Roy. Sci. Liege, 88, 166
Johnston, K. G., Shepherd, D. S., Robitaille, T. P., & Wood, K. 2013, A&A, 551, A43
Knödlseder, J. 2000, A&A, 360, 539
Kohoutek, L. 2001, A&A, 378, 843
Kryukova, E., Megeath, S. T., Hora, J. L., et al. 2014, AJ, 148, 11
Lu, X., Zhang, Q., Liu, H. B., Wang, J., & Gu, Q. 2014, ApJ, 790, 84
Magliocchetti, M., Maddox, S. J., Lahav, O., & Wall, J. V. 1998, MNRAS, 300, 257
Mahy, L., Rauw, G., De Becker, M., Eenens, P., & Flores, C. A. 2013, A&A, 550, A27
Martí, J., Pérez-Ramírez, D., Luque-Escamilla, P., et al. 2006, A&A, 451, 1037
Melikian, N. D., Tamazian, V. S., Karapetian, A. A., Samsonian, A. L., & Kostandian, G. R. 2011, Astrophysics, 54, 203
Massaro, F., D'Abrusco, R., Giroletti, M., et al. 2013, ApJS, 207, 4
Mitronova, S. N., Karachentsev, I. D., Karachentseva, V. E., Jarrett, T. H., & Kudrya, Y. N. 2004, Bull. Spec. Astrophys. Obs., 57, 5
Montes, V. A., Hofner, P., Anderson, C., & Rosero, V. 2015, ApJS, 219, 41
Neria, C., Gómez, Y., & Rodríguez, L. F. 2010, Rev. Mex. Astron. Astrofis., 46, 253
Panessa, F., Tarchi, A., Castangia, P., et al. 2015, MNRAS, 447, 1289
Paredes, J. M., Martí, J., Ishwara-Chandra, C. H., et al. 2008, A&A, 482, 247
Parthasarathy, M., Jain, S. K., & Bhatt, H. C. 1992, A&A, 266, 202
Paunzen, E. 2015, A&A, 580, A23
Price-Whelan, A. M., Hogg, D. W., Rix, H.-W., et al. 2018, AJ, 156, 18
Purcell, C. R., Hoare, M. G., Cotton, W. D., et al. 2013, ApJS, 205, 1
Ramachandran, V., Das, S. R., Tej, A., et al. 2017, MNRAS, 465, 4753
Rauw, G. 2011, A&A, 536, A31
Reddish, V. C., Lawrence, L. C., & Pratt, N. M. 1966, Publ. Roy. Obs. Edinburgh, 5, 111
Reipurth, B., & Schneider, N. 2008, Star Formation and Young Clusters in Cygnus, ed. B. Reipurth (ASP), 36
Rengelink, R. B., Tang, Y., de Bruyn, A. G., et al. 1997, A&AS, 124, 259
Rodríguez-Kamenetzky, A., Carrasco-González, C., González-Martín, O., et al. 2019, MNRAS, 482, 4687
Romero, G. 2008, in Gamma Rays from Star Forming Regions, ed. F. A. Aharonian (AIP), 97
Romero, G. E., Torres, D. F., Kaufman Bernadó, M. M., & Mirabel, I. F. 2003, A&A, 410, L1
Sánchez-Monge, Á., Palau, A., Estalella, R., Beltrán, M. T., & Girart, J. M. 2008, A&A, 485, 497
Scaife, A. M. M., & Heald, G. H. 2012, MNRAS, 423, L30
Setia Gunawan, D. Y. A., de Bruyn, A. G., van der Hucht, K. A., & Williams, P. M. 2003, ApJS, 149, 123
Solin, O., Ukkonen, E., & Haikala, L. 2012, A&A, 542, A3
Swarup, G., Ananthakrishnan, S., Kapahi, V. K., et al. 1991, Curr. Sci., 60, 95
Taylor, A. R., Goss, W. M., Coleman, P. H., van Leeuwen, J., & Wallace, B. J. 1996, ApJS, 107, 239
The Fermi-LAT collaboration 2020, ApJS, 247, 33
Urquhart, J. S., Hoare, M. G., Purcell, C. R., et al. 2009, A&A, 501, 539
Uyanıker, B., Fürst, E., Reich, W., Aschenbach, B., & Wielebinski, R. 2001, A&A, 371, 675
Verbeek, K., Groot, P. J., Scaringi, S., et al. 2012, MNRAS, 426, 1235
Véron-Cetty, M. P., & Véron, P. 2010, A&A, 518, A10
Vollmer, B., Gassmann, B., Derrière, S., et al. 2010, A&A, 511, A53
Wendker, H. J., Higgs, L. A., & Landecker, T. L. 1991, A&A, 241, 551
Williams, P. K. G., Bower, G. C., Croft, S., et al. 2013, ApJ, 762, 85
Wright, N. J., Drake, J. J., Drew, J. E., et al. 2012, ApJ, 746, L21
Zhang, Q., Claus, B., Watson, L., & Moran, J. 2017, ApJ, 837, 53
Zoonematkermani, S., Helfand, D. J., Becker, R. H., White, R. L., & Perley, R. A. 1990, ApJS, 74, 181

Appendix A: Additional table

Table A.1. Counterparts of detected sources at 325 MHz and 610 MHz.

325-ID BIC325-	610-ID BIC610-	Spectral index	RA_{J2000} (h,m,s)	Dec_{J2000} (deg,′,″)	d (″)	SIMBAD nearest source	Reference	Information on possible nature
——	0045	——	20:12:57.27	41:51:49.34	4.6	2MFGC 15386	Mitronova et al. (2004)	Disk-like galaxy
——	0093	——	20:13:47.77	41:10:02.13	7.6	CXO J201348.3+411007.1	Montes et al. (2015)	X-ray source
0006	0124	−1.0 ± 0.1	20:14:18.68	41:18:11.26	5.4	CXO J201419.1+411813.4	Montes et al. (2015)	Star-forming region
——	0217	——	20:15:21.60	40:34:43.93	6.8	PN KjPn 2	Kohoutek (2001)	Planetary nebula
0107	0429	−1.0 ± 0.3	20:17:54.12	41:24:14.49	5.3	J201754.59+412413.98	Kryukova et al. (2014)	IR source
0119	0462	−1.6 ± 0.2	20:18:07.79	41:10:41.13	5.2	FGL J2018.1+4111	Abeysekara et al. (2018)	γ-ray source
0134	0531	−2.4 ± 0.1	20:18:38.18	40:41:00.42	3.7	MSX6C G078.0875+02.6408	Panessa et al. (2015)	Seyfert galaxy
——	0543	——	20:18:42.69	44:17:34.13	2.2	NVSS J201842+441736	Vollmer et al. (2010)	
——	0551	——	20:18:46.65	42:20:04.91	8.2	NVSS J201847+422010	Condon et al. (1998)	
——	0582	——	20:19:02.55	40:18:26.02	4.1	WSRTGP 2017+4009	Vollmer et al. (2010)	
0151	0624	−0.2 ± 0.3	20:19:19.30	40:54:51.52	7.8	MTK2011–F1 14	Melikian et al. (2011)	Emission-line star
0162/0163/0164	0665/0666/0672	−1.0 ± 0.2	20:19:36.50	40:58:50.00	∼10	NGR2010–VLAN 2,3	Neria et al. (2010)	UC HII region
0165	0676	+0.9 ± 0.1	20:19:38.89	40:56:36.21	1.3	IRAS 20178+4046–VLAN 4	Neria et al. (2010)	UC HII region
0170	0690	−1.0 ± 0.1	20:19:49.33	42:00:12.26	5.0	J201949.77+420011.20	Kryukova et al. (2014)	YSO
——	0731	——	20:20:09.10	43:40:22.78	2.0	RX J2020.0+4357	Brinkmann et al. (1997)	X-ray source
0182	0757	+0.1 ± 0.2	20:20:18.62	40:58:03.26	5.3	J202019.08+405802.18	Kryukova et al. (2014)	YSO
——	0787	——	20:20:27.95	43:51:13.88	2.4	WR 140	De Becker & Raucq (2013)	WR system
0196	0808	+0.3 ± 0.1	20:20:35.65	40:57:54.84	6.2	J202036.15+405753.58	Kryukova et al. (2014)	YSO
″	″	″	20:20:36.18	40:57:53.08	6.6	NVSS J202036+405754	Vollmer et al. (2010)	
——	0825	——	20:20:42.59	42:16:46.54	8.0	MITG J2020+4216	Vollmer et al. (2010)	
0200	0842	−0.0 ± 0.3	20:20:51.07	41:22:05.96	5.6	J202051.55+412204.76	Kryukova et al. (2014)	YSO
——	0861	——	20:20:57.67	44:41:29.82	0.9	NVSS J202057+444130	Vollmer et al. (2010)	
——	0894	——	20:21:18.24	41:19:59.65	5.0	J202118.68+411958.86	Kryukova et al. (2014)	YSO
——	0967	——	20:21:49.02	44:00:37.37	2.7	2MASX J20214907+4400399	Véron-Cetty & Véron (2010)	Seyfert galaxy
——	1049	——	20:22:17.22	42:24:49.47	10.4	18P 22	Vollmer et al. (2010)	
0263	1051	−0.1 ± 0.2	20:22:17.85	43:53:01.09	8.3	2MASS J20221736+4353074	Price-Whelan et al. (2018)	Red giant star
——	1112	——	20:22:44.55	41:45:17.41	5.9	J202245.07+414517.98	Kryukova et al. (2014)	YSO
——	1117	——	20:22:46.33	41:07:00.44	5.8	J202245.07+414517.98	Kryukova et al. (2014)	YSO
——	1126	——	20:22:52.35	44:48:20.56	3.3	BD+44 3444	Elyajouri et al. (2016)	B8 star
——	1205	——	20:23:19.06	43:12:44.08	8.2	IRAS 20216+4303	Vollmer et al. (2010)	
0343	1248	+0.1 ± 0.1	20:23:35.68	41:25:26.43	3.3	J202335.81+412523.53	Kryukova et al. (2014)	YSO
0347	1253	−0.8 ± 0.1	20:23:39.05	44:01:04.49	10.6	18P 25	Vollmer et al. (2010)	
0393	1329	−1.2 ± 0.2	20:24:11.53	41:43:24.47	9.1	TYC 3160–519–1	Høg et al. (2000)	Star
0390/0395	1334	−0.5 ± 0.1	20:24:15.43	43:22:32.22	5	NVSS J202415+432235	Vollmer et al. (2010)	
0434	1404	−0.6 ± 0.3	20:24:46.19	42:23:13.16	9.3	BD+41 3737	Paunzen (2015)	Star
——	1420	——	20:24:52.00	40:40:25.21	5.6	G078.779+01.693	Anderson et al. (2015)	HII region
0460	1447	−0.7 ± 0.1	20:25:00.59	41:48:25.43	6.1	NVSS J202501+414829	Condon et al. (1998)	
0490	1493	+0.6 ± 0.1	20:25:19.02	43:35:19.40	4.7	J2025+4335	Immer et al. (2011)	
0496	1503	−0.8 ± 0.1	20:25:22.74	44:19:33.44	1.4	NVSS J202522+441934	Condon et al. (1998)	
0503	1511	−0.8 ± 0.2	20:25:24.78	41:03:19.48	3.6	G079.151+01.830	Solin et al. (2012)	Star-forming region
0526	1557/1563	−1.1 ± 0.1	20:25:40.53	42:32:17.14	6.4	NVSS J202540+423222	Condon et al. (1998)	
——	1569	——	20:25:42.91	41:56:15.55	5.6	NVSS J202543+415618	Vollmer et al. (2010)	
——	1572	——	20:25:44.10	41:56:02.14	6.0	J202544.53+415605.70	Kryukova et al. (2014)	YSO
0600	1680	−1.0 ± 0.1	20:26:25.48	42:32:09.42	5.2	NVSS J202625+423214	Condon et al. (1998)	
0604	1685	−0.8 ± 0.1	20:26:26.26	44:39:27.16	3.9	NVSS J202625+443927	Vollmer et al. (2010)	
0626	1728	−0.9 ± 0.1	20:26:42.98	40:51:28.03	10.5	NVSS J202642+405138	Vollmer et al. (2010)	
——	1821	——	20:27:18.99	40:25:00.97	1.0	WSRTGP 2025+4015	Vollmer et al. (2010)	
0684	1822	−1.1 ± 0.1	20:27:19.57	43:13:58.44	14.3	TYC 3164–341–1	Høg et al. (2000)	Star
0722	1908	−0.8 ± 0.1	20:27:52.92	41:35:05.03	5.2	J202753.37+413506.03	Kryukova et al. (2014)	IR source
0735	1944	−0.4 ± 0.1	20:28:04.06	41:13:54.24	5.1	J202804.51+411354.56	Kryukova et al. (2014)	YSO
0744	1957	−0.8 ± 0.1	20:28:07.20	41:13:50.64	7.9	UVEX J202807.55+411357.7	Verbeek et al. (2012)	White dwarf
——	1967	——	28:28:10.38	45:12:51.73	0.2	NVSS J202810+451251	Condon et al. (1998)	
——	1980	——	20:28:13.29	40:16:52.83	3.6	WSRTGP 2026+4006	Vollmer et al. (2010)	
0769	2013	−1.1 ± 0.1	20:28:24.34	40:37:50.03	3.9	19P 6	Wendker et al. (1991)	
——	2027	——	20:28:31.01	40:59:59.05	3.9	J202831.35+405959.24	Kryukova et al. (2014)	YSO
0788	2068	−1.1 ± 0.1	20:28:49.60	41:18:37.36	0.6	TYC 3160–1079–1	Høg et al. (2000)	Star
0789	2070	−1.3 ± 0.1	20:28:50.79	41:34:37.13	5.5	NVSS J202851+413438	Vollmer et al. (2010)	
0804	2108	−1.1 ± 0.1	20:29:00.90	42:12:59.28	5.5	NVSS J202901+421259	Condon et al. (1998)	
0806	2115	−0.9 ± 0.1	20:29:04.20	41:00:05.78	4.1	19P 7	Wendker et al. (1991)	
0807	2118	−1.0 ± 0.1	20:29:04.70	42:35:27.90	4.4	TYC 3160–1447–1	Høg et al. (2000)	Star
——	2159	——	20:29:23.53	40:11:09.57	4	AFGL 2591	Johnston et al. (2013)	Star-forming region
——	2170	——	20:29:28.60	40:57:24.41	7.0	19P 9	Wendker et al. (1991)	
——	2174	——	20:29:30.94	41:34:20.72	5.2	J202931.39+413421.96	Kryukova et al. (2014)	YSO
——	2189	——	20:29:36.50	41:51:40.89	4.6	WSRTGP 2027+4141	Vollmer et al. (2010)	

Table A.1. continued.

325-ID BIC325-	610-ID BIC610-	Spectral index	RA_{J2000} (h, m, s)	Dec_{J2000} (deg,′,″)	d (″)	SIMBAD nearest source	Reference	Information on possible nature
0846	2215	−1.7 ± 0.3	20:29:49.42	41:43:13.66	16.7	** GRV 344	Greaves (2004)	Stellar system
—	2223	—	20:29:52.06	40:48:45.82	2.7	G079.4430+01.0047	Urquhart et al. (2009)	HII region
0854	—	—	20:29:59.18	41:16:44.20	7.0	IRAS 20286+4105	Ramachandran et al. (2017)	Star-forming region
0867	2280	−0.9 ± 0.1	20:30:14.17	40:41:08.67	10.4	IRAS 20283+4031	Parthasarathy et al. (1992)	Star
0872	2299	−1.2 ± 0.1	20:30:30.47	44:12:26.40	4.9	2MASS J20303018+4412301	Price-Whelan et al. (2018)	Star
0873	2311	−0.7 ± 0.1	20:30:36.58	41:06:06.10	6.2	NVSS J203032+410634	Williams et al. (2013)	
—	2313	—	20:30:37.68	42:20:57.96	15.9	WSRTGP 2028+4211	Vollmer et al. (2010)	
0874	2319	−0.8 ± 0.1	20:30:39.72	41:23:31.73	0.4	NVSS J203039+412331	Vollmer et al. (2010)	
—	2351	—	20:30:57.60	43:08:05.33	6.9	WSRTGP 2029+4257	Vollmer et al. (2010)	
0882	2370	−2.1 ± 0.3	20:31:10.22	40:58:53.80	2.5	J203110.44+405853.94	Kryukova et al. (2014)	YSO
—	2376	—	20:31:14.29	42:22:42.95	4.1	TYC 3161–82–1	Høg et al. (2000)	Star
0889	2381	−1.0 ± 0.2	20:31:18.69	41:09:25.16	10.7	RLP 933	Reddish et al. (1966)	Star
—	2382	—	20:31:19.14	40:18:09.90	0.4	IRAS 20293+4007 VLA 3	Sánchez-Monge et al. (2008)	
0890	2384	−1.0 ± 0.1	20:31:19.90	40:40:56.04	1.6	GPSR 079.501+0.704	Zoonematkermani et al. (1990)	
—	2406	—	20:31:37.33	40:22:58.79	0.3	G79.29+0.46	Higgs et al. (1994)	Wind shell
—	2409	—	20:31:39.72	40:16:08.36	0.2	G79.29+0.46	Higgs et al. (1994)	Wind shell
—	2420	—	20:31:51.59	41:31:18.60	2.8	BDB2006–234	Paredes et al. (2008)	X-ray star
0906	2432	−1.4 ± 0.1	20:32:00.50	41:36:58.45	1.0	J203201.7+413722	Paredes et al. (2008)	Galaxy S lobe
0908	2435	−1.4 ± 0.1	20:32:01.91	41:37:47.43	1.0	J203201.7+413722	Paredes et al. (2008)	Galaxy N lobe
0915	2448	−2.1 ± 0.4	20:32:12.92	41:27:24.01	2.3	MT91–213	Chen et al. (2019)	Be star+pulsar
—	2452	—	20:32:14.13	40:42:24.88	0.7	NVSS J203214+404226	Vollmer et al. (2010)	
—	2463	—	20:32:21.17	40:17:18.63	0.5	DR 15 I	Colley (1980)	Part of nebula
0921	2464	−0.5 ± 0.2	20:32:22.32	41:18:19.28	1.2	Cyg OB2 5	De Becker & Raucq (2013)	OB stellar system
0924	2469	+1.4 ± 0.1	20:32:25.65	40:57:28.09	1.5	WR 145a	Bulgarelli et al. (2019)	HMXB
0925	2470	−0.5 ± 0.1	20:32:26.77	41:04:33.28	1.3	HSC N	Martí et al. (2006)	Part of cloud
0927	2472	−1.3 ± 0.2	20:32:29.25	41:35:07.36	1.7	2MASS J20322935+4135061	Cutri et al. (2003)	IR source
0928	2473	−0.1 ± 0.3	20:32:29.52	40:38:49.65	0.9	GPSR 079.602+0.506	Zoonematkermani et al. (1990)	
0933	—	—	20:32:36.60	41:14:47.87	14.4	RLP 886	Reddish et al. (1966)	Star
—	2494	—	20:32:40.83	41:14:29.31	1.4	Cyg OB2 12	De Becker & Raucq (2013)	Star
0941	2501	+0.6 ± 0.1	20:32:45.44	40:39:37.50	1.3	EM* MWC 349	Zhang et al. (2017)	Emission-line star
0946	2514	−0.9 ± 0.1	20:32:55.32	40:31:30.99	4.6	19P 22	Wendker et al. (1991)	
0953	2526	−1.1 ± 0.1	20:33:10.27	40:41:16.91	1.9	J203310.31+404118.72	Kryukova et al. (2014)	YSO
″	2528	″	20:33:11.01	40:41:32.23	4.8	19P 24	Vollmer et al. (2010)	
″	2530	″	20:33:11.74	40:41:49.35	2.1	J203311.80+404151.32	Kryukova et al. (2014)	YSO
—	2536	—	20:33:14.93	41:18:50.63	1.7	Cyg OB2 8A	De Becker & Raucq (2013)	OB stellar system
0956	2544/2545	−0.3 ± 0.1	20:33:18.92	40:58:37.39	14.4	G079.964+00.579	Anderson et al. (2015)	
0957	2545	−0.4 ± 0.1	20:33:19.00	40:59 05.06	13.6	G079.964+00.579	Anderson et al. (2015)	
″	—	—	20:33:19.00	40:59 05.06	15.5	BD+40 4230	Reddish et al. (1966)	Star
0963	2552/2556/2558	−1.2 ± 0.1	20:33:23.42	41:27:17.60	6.6	19P 26	Vollmer et al. (2010)	
″	″	″	20:33:23.42	41:27:17.60	22.3	IDX 114	Rauw (2011)	X-ray star
0965	2559	−0.8 ± 0.3	20:33:24.95	40:57:28.81	8.3	RLP 1034	Reddish et al. (1966)	Star
0966	2560	−0.5 ± 0.3	20:33:26.58	40:42:33.04	1.8	J203326.44+404233.74	Kryukova et al. (2014)	YSO
—	2565	—	20:33:30.74	41:35:28.42	8.5	RLP 283	Reddish et al. (1966)	Star
0968	2566	−0.3 ± 0.1	20:33:31.97	40:41:03.03	8.2	19P 28	Wendker et al. (1991)	
0976	2585	−1.4 ± 0.1	20:33:47.12	40:40:54.64	10.6	J203348.01+404051.61	Kryukova et al. (2014)	YSO
0977	2589	−0.9 ± 0.1	20:33:52.22	41:15:45.11	7.7	AFM2007–990	Albacete Colombo et al. (2007)	X-ray star
—	2603	—	20:34:06.69	41:16:00.86	1.0	J203406.77+411600.46	Kryukova et al. (2014)	YSO
0985	2607	−0.3 ± 0.2	20:34:10.56	41:06:58.71	0.7	IPHASX J203410.5+410659	Wright et al. (2012)	frEGG
0988	2610	−2.5 ± 0.2	20:34:13.85	41:08:16.31	5.0	WDDGGHK7	Isequilla et al. (2019)	frEGG
1000	2635	−1.6 ± 0.2	20:34:36.48	40:51:59.24	5.3	WDDGGHK4	Isequilla et al. (2019)	frEGG
1003	2638	−1.3 ± 0.1	20:34:43.28	40:53:15.48	2.1	WDDGGHK3	Isequilla et al. (2019)	frEGG
—	2652	—	20:34:53.33	40:53:20.89	2.2	WDDGGHK2	Isequilla et al. (2019)	frEGG
1006	2641	−0.8 ± 0.3	20:34:45.15	41:45:03.2	3.2	GPSR 079.918+0.283	Zoonematkermani et al. (1990)	
—	2625	—	20:34:29.54	41:31:45.2	0.7	TYC 3161–1048–1	Høg et al. (2000)	star
1012	2654	−0.6 ± 0.1	20:34:55.80	40:40:46.56	1.6	GPSR 079.904+0.154	Zoonematkermani et al. (1990)	
—	2657	—	20:34:57.30	40:04:14.94	6.5	TYC 3157–1182–1	Høg et al. (2000)	Star
1014	2659	+0.4 ± 0.1	20:35:00.28	41:34:52.90	2.34	IRAS 20332+4124	Lu et al. (2014)	Star-forming region
1018	2663	−0.0 ± 0.2	20:35:02.77	41:34:51.22	10.8	IRAS 20332+4124	Lu et al. (2014)	Star-forming region
1019	2664	−0.1 ± 0.2	20:35:03.56	41:18:24.12	0.4	2MASS J20350353+4118240	Cutri et al. (2003)	IR source
—	2666	—	20:35:07.84	39:59:48.46	2.8	GPSR 079.380−0.284	Zoonematkermani et al. (1990)	
1020	2670	+0.9 ± 0.1	20:35:16.63	40:49:44.66	1.0	GPSR 080.063+0.191	Zoonematkermani et al. (1990)	
1024	2680	−1.2 ± 0.1	20:35:32.37	41:44:56.33	0.8	NVSS J203532+414456	Condon et al. (1998)	

Table A.1. continued.

325-ID BIC325-	610-ID BIC610-	Spectral index	RA_{J2000} (h, m, s)	Dec_{J2000} (deg,′,″)	d (″)	SIMBAD nearest source	Reference	Information on possible nature
1025	——	——	20:35:33.17	41:06:45.07	2.8	GPSR 080.322+0.319	Vollmer et al. (2010)	
1027	——	——	20:35:42.72	40:52:51.58	1.7	GPSR 080.154+0.156	Zoonematkermani et al. (1990)	
1030	2689	+0.2 ± 0.2	20:35:47.07	41:22:45.01	0.4	WR 146	De Becker & Raucq (2013)	WR system
——	2693	——	20:35:55.32	42:18:03.67	3.5	2034+42A	Clegg et al. (1992)	
——	2697	——	20:35:58.48	42:17:23.86	3.1	2034+42B	Clegg et al. (1992)	
1032	2698	−0.6 ± 0.2	20:35:59.52	40:54:00.86	12.5	J203558.60+405353.85	Kryukova et al. (2014)	YSO
″	″	″	20:36:01.31	40:53:56.79	4.4	J203600.94+405358.24	Kryukova et al. (2014)	YSO
″	2700	″	20:36:01.31	40:53:56.79	8.1	J203601.85+405351.48	Kryukova et al. (2014)	YSO
1034	2707	+0.2 ± 0.2	20:36:12.84	40:45:43.14	2.1	GPSR 080.115+0.009	Zoonematkermani et al. (1990)	
1038	2721	−0.6 ± 0.1	20:36:29.72	41:20:21.90	0.5	CPR2002–B3	Comerón et al. (2002)	Star
1039	2722	−1.2 ± 0.1	20:36:34.45	41:32:22.66	10.9	G080.522+00.714	Zoonematkermani et al. (1990)	
——	2730	——	20:36:43.72	40:21:09.99	2.6	WR 147	De Becker & Raucq (2013)	WR system
——	2770	——	20:37:37.72	40:53:52.54	1.8	080.386−0.122	Garwood et al. (1988)	
——	2785	——	20:37:58.29	40:00:52.85	2.9	18P 6	Vollmer et al. (2010)	
——	2793	——	20:38:22.23	40:16:16.95	2.0	GPSR 079.972−0.614	Zoonematkermani et al. (1990)	